

Interweaving polar charge orders in a layered metallic super-atomic crystal

Shuya Xing^{1,+}, Linlu Wu^{1,+}, Zilu Wang^{1,+}, Xu Chen^{2, +}, Haining Liu^{3,4}, Shuo Han¹, Le Lei¹, Linwei Zhou¹, Qi Zheng^{2,4}, Li Huang^{2,4}, Xiao Lin⁴, Shanshan Chen¹, Liming Xie^{3,4}, Xiaolong Chen^{2,4,5}, Hong-Jun Gao^{2,4}, Zhihai Cheng^{1,*}, Jiangang Guo^{2,5,*}, Shancai Wang^{1,*}, and Wei Ji^{1,*}

¹*Beijing Key Laboratory of Optoelectronic Functional Materials & Micro-nano Devices,
Department of Physics, Renmin University of China, Beijing 100872, China*

²*Beijing National Laboratory for Condensed Matter Physics, Institute of Physics, Chinese
Academy of Sciences, P.O. Box 603, Beijing 100190, China.*

³*CAS Key Laboratory of Standardization and Measurement for Nanotechnology, CAS Centre
for Excellence in Nanoscience, National Centre for Nanoscience and Technology, Beijing
100190, China*

⁴*University of Chinese Academy of Sciences, Beijing 100039, China*

⁵*Songshan Lake Materials Laboratory, Dongguan, Guangdong 523808, China*

Abstract: Electronic properties of super-atomic crystals are far from being well explored in the case of their versatile building units and premature understanding of their inter-unit couplings. Here, we experiment-theory jointly investigated a rational-designed layered super-atomic crystal of $\text{Au}_6\text{Te}_{12}\text{Se}_8$ cubes, stacked through non-covalent inter-cube quasi-bonds. We found a sequential-emerged anisotropic triple-cube charge-density-wave and spatially polarized metallic states below 120 K, as examined using scanning tunneling microscopy/spectroscopy, angle-resolved photoemission spectroscopy, transport measurement, Raman spectra and density functional theory. The polarized states are locked in an anti-parallel configuration, required by maintaining the inversion symmetry of the center-cube of a tri-cube group. The anti-polar metallic states are thus interwoven by the charge density wave and the polarized metallic states, primarily ascribed to electronic effects rather than atomic displacements. This work demonstrated that strong electronic interactions could play an essential role in determining electronic properties of non-covalent super-atomic solids, which shed considerable light on expanding the existing category of quantum materials to non-covalent solids.

⁺ These authors contributed equally: Shuya Xing, Linlu Wu, Zilu Wang, Xu Chen.

* Email: zhihaicheng@ruc.edu.cn jguo@iphy.ac.cn scw@ruc.edu.cn wji@ruc.edu.cn

Introduction

Synthesis of emergent crystals is the foundation of discovering novel phenomena, exploring intriguing properties and uncovering previously unknown principles in research of, e.g. Iron-based superconductors ($\text{La}[\text{O}_{1-x}\text{F}_x]\text{FeAs}$)¹, perovskite solar cells ($\text{CH}_3\text{NH}_3\text{PbI}_3$ ^{2,3} and $\text{CH}_3\text{NH}_3\text{PbBr}_3$ ⁴), two-dimensional magnetism (CrI_3)⁵⁻⁷ and among the others. However, it was inherently limited that subsequent optimization of those crystals, e.g. $\text{La}[\text{O}_{1-x}\text{F}_x]\text{FeAs}$, by altering one type of atoms with another. The limited number of 82 stable and non-radioactive elements aside, each of them has its intrinsic characteristics that governs which other atoms it could chemically bond to. Thus, substitution of a new type of atoms usually introduces different structures with largely varied properties^{9,10}, which poses an overwhelming challenge to rational design of functional materials^{11,12}.

Non-covalent, e.g. van der Waals (vdW), interactions seem a cure for this challenge. Stacking of two-dimensional (2D) monolayers through vdW attractions usually introduces interlayer wavefunction overlap with subsequent electronic hybridization. It was previously known as covalent-like quasi-bonding (CLQB) as the overlapped wavefunction yields a covalent-like charge redistribution characteristic at the interlayer region¹³⁻¹⁶. Such CLQB offers a route to drastically change bandgaps^{13,14}, optical transitions^{15,16}, topological properties¹⁷, magnetism^{18,19}, electrical polarization²⁰, superconductivity^{10,21} and among the others of 2D few-layers by, e.g. stacking²², twisting²³, bending²⁴ and compressing²⁵, which show much higher feasibility and tuning potential compared with traditional bulk crystals.

In spite of huge success achieved in building novel 2D homo- and hetero-structures, covalent bonding still governs the in-plane position and type of atoms in each monolayer. An even aggressive strategy lies in introducing in-plane non-covalent bonding, namely, using atomic clusters, instead of atoms, as building blocks to construct layered materials through non-covalent bonding. Those atomic clusters are also known for super-atoms^{12,26-30}, which have, in principle, countless species available for materials design^{12,29,30}. Super-atomic crystals could be assembled through various linkages that usually result in weak inter-super-atom electronic interactions^{12,26-30}. As

an emergent linkage, π - π CLQB helps with forming free-electron-like bands in pentacene³¹ and C₆₀ monolayers^{32,33} under finely tuned compression. Nevertheless, electrons in those monolayers were well described in a single-particle picture, apart from strong electron-electron or electron-quasiparticle interactions which are the origin of many intriguing and complicated physical phenomena³⁴⁻³⁶, e.g. charge density wave (CDW) and superconductivity, observed in quantum materials.

Here, we show experimental evidence for strong electronic interactions in a rationally designed layered material of high-symmetry, cubically shaped Au₆Te₁₂Se₈ (ATS) super-atomic crystal (Fig.1), which offers up-to 12 Te...Te CLQBs and was found to be superconducting below \sim 2.8 K^{37,38}. The Te...Te quasi-bonding appears an enthralling non-covalent interaction in terms of small energy cost, high tunability and strong electronic coupling, as illustrated in layered Te allotropes^{39,40}. The surface electronic structures and electrical properties of ATS were revealed using low-temperature scanning tunneling microscope (LT-STM), angle-resolved photoemission spectroscopy (ARPES) together with Raman and transport measurements, and density functional theory (DFT) calculations. We found two charge orders on the cleaving surface, namely a triple-cube-width stripe period along the *a*-axis and a spontaneous electric polarization with interlocked anti-polar directions along the *b*-axis, which were explained in a strong Coulomb interaction picture. The strongly electronically coupled super-atom layers opens a category of layered materials for exhibiting manipulatable novel properties in tremendous layered structures with high and precise tunability.

Results and discussion

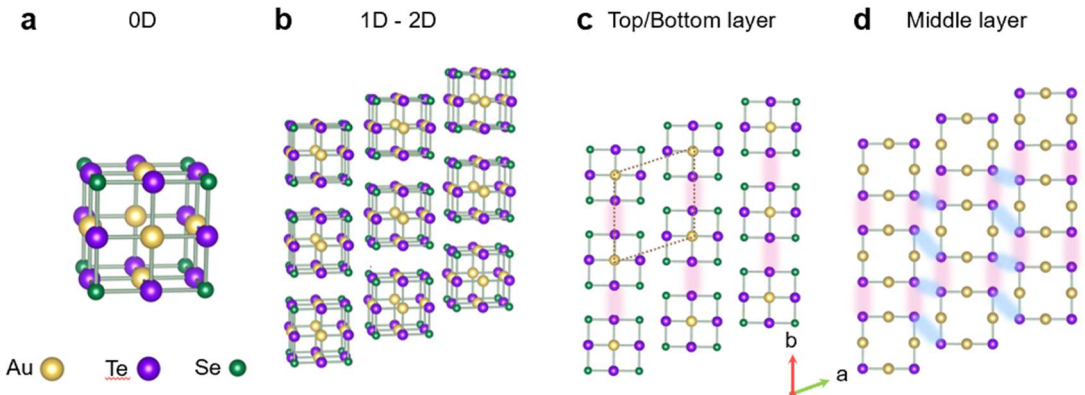


Figure 1. Atomic structures and inter-cube interactions of the $\text{Au}_6\text{Te}_{12}\text{Se}_8$ (ATS) super-atomic crystal. **a**, Individual ATS cube, regarded as a super-atom (0D). **b**, Atomic structure of an ordered ATS monolayer cleaved from an ATS bulk crystal, in which ATS cubes form one-dimensional (1D) chains along the *b*-axis. Top views for the slabs of the top/bottom (**c**) and middle (**d**) sub-layers of the ATS monolayer, in which red and blue shadowed lines illustrate intra- (red) and inter-chain (blue) inter-cube $\text{Te}\dots\text{Te}$ interactions, respectively. Yellow, purple and green balls represent Au, Te and Se atoms, respectively.

Super-atomic crystal and CLQBs

An ATS super-atom is comprised of orderly arranged Au, Te and Se atoms showing a cube-like high-symmetric geometry, in which those three types of atoms are located at the faces, edges and corners, respectively (Fig. 1a). The lattice of a three-dimensional ATS super-atomic crystal possibly reduces its symmetry, showing the *P2* (*P211*) symmetry on a cleaving surface in the *a*-*b* plane (Supplementary Fig. S1). In this plane, those cubes form one-dimensional (1D) chains along the *b*-axis (the chain direction was originally defined as the *a*-axis in the bulk crystal) and they slightly slide across chains (Fig. 1b and Supplementary Fig. S2). These super-atoms are more flexible to bond with each other than traditional atoms, like Te, which allows to form complicated and highly tunable 2D $\text{Te}\dots\text{Te}$ quasi-bonding networks. In particular, there are four $\text{Te}\dots\text{Te}$ non-covalent quasi-bonds (red shadowed lines in Fig. 1c and 1d), i.e. two in the top and bottom sub-layers (Fig. 1c) and the other two in the middle sub-layer (Fig. 1d), which participate in the formation of ATS chains through non-covalent interactions. Two additional $\text{Te}\dots\text{Te}$ bonds (blue shadowed lines in Fig. 1d) were found only in the middle sub-layer, suggesting strong anisotropy of inter-cube interactions in the surface ATS

layer (Supplementary Fig. S3). The inter-cube Te...Se and Te...Au interactions are substantially weaker than inter-cube Te...Te bonding and away from the Fermi level, which are out of focus in the present work.

Two sequential-emerged charge orders

Figure 2a plots the measured temperature-dependent resistivity and its first-order derivative of an ATS flake sample. A nearly linear relation was observed before the sample cooling down to 80 K where an abrupt change occurs, suggesting the emergence of a likely charge order⁴¹. As the temperature further decreased, a superconducting transition characteristic appears at ~2.8 K (Supplementary Fig. S4)³⁷. The likely charge order transition at 80 K seems nonsynchronous with the geometrical transition, as indicated by a temperature-dependent Raman shift measurement (Fig. 2b). While Raman peak at 20 cm⁻¹ (RP1) fades out during the cooling-down process, a new peak (RP2) emerges and gradually blue shifts. The position of RP2 eventually maintains at ~205 cm⁻¹ below 120K. It is thus of interest to uncover the reason why both macroscopic measurements reveal different transition temperatures.

Figure 2c-2f show a series of temperature-dependent STM images and their corresponding FFT patterns acquired at 80, 100, 120 and 150 K, respectively, explicitly showing two charge orders. In particular, the image acquired at 150 K (Fig. 2f) shows a chain-like appearance, indicating no charge modulation, while the chain-like pattern confirms the expected anisotropic inter-cube interactions. A triple-chain-width, stripe-like charge modulation fades in at ~120 K (Fig. 2e) and becomes clearer at ~100 K (Fig. 2d). An additional order emerges along the *a*-axis when the temperature decreases to ~80 K, which was more closely examined in a zoomed-in STM topographic image acquired at 9 K (Fig. 2g). The STM measured surface lattice constants of *a*=9.08 Å and *b*=9.32 Å are very close to those of DFT values of *a*=9.02 Å and *b*=9.28 Å, respectively. The STM image shows multiple chain-like features parallel to the *b*-axis. Its FFT pattern confirms the stripe width of three ATS chains according to the observed characteristic peak ($q^* = a^*/3$) in the *a*^{*} axis.

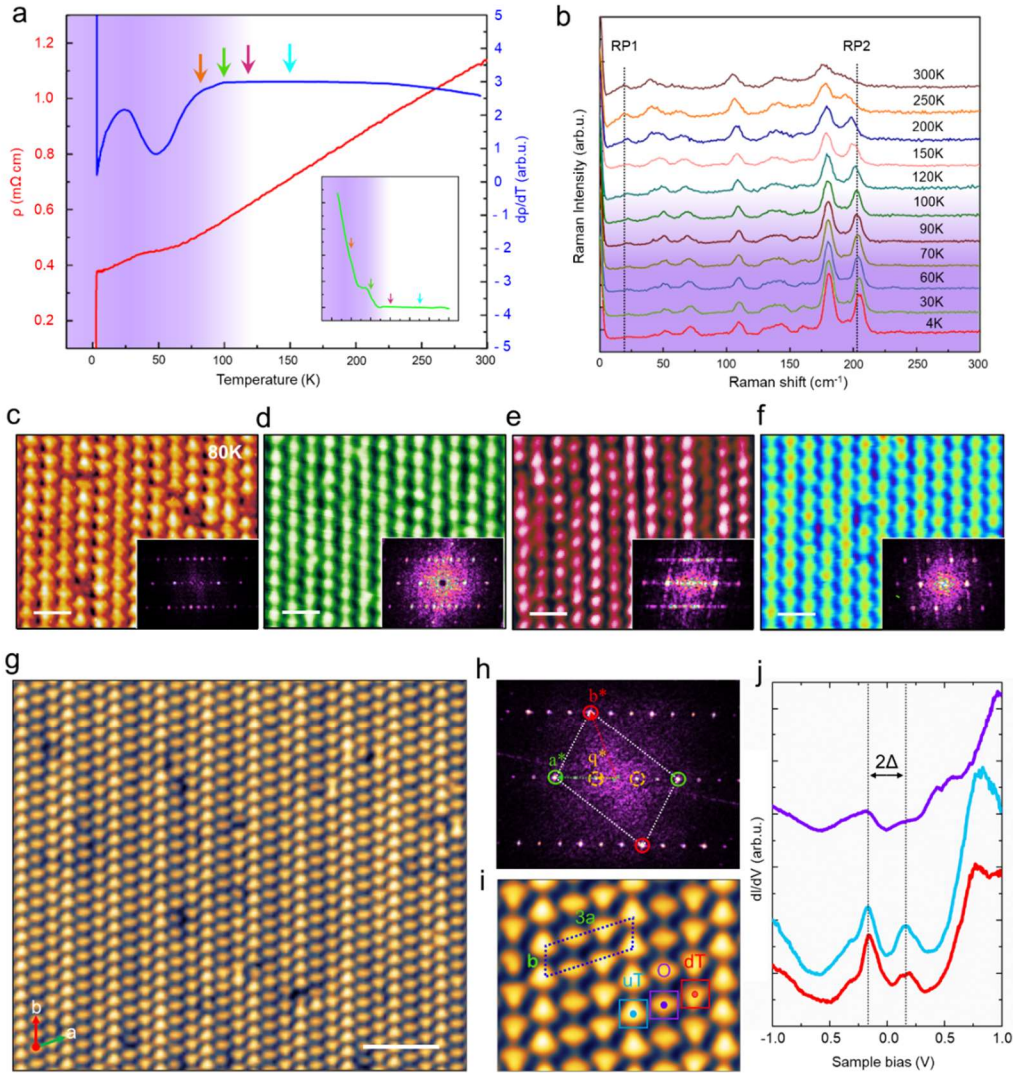


Figure 2. Charge order transitions in the ATS super-atomic crystal. **a**, Temperature-dependent resistivity (red) and its derivative (blue) curves. The insert is the second order derivative (green) curves around the charge order transition. **b**, Temperature-dependent Raman spectrum. A new Raman peak emerged and gradually blue shifted with the decreased temperatures, and maintained at ~ 205 cm^{-1} below 120K. **c-f**, STM topography and the corresponding FFT patterns obtained at temperatures of 80 K (**c**), 100 K (**d**), 120 K (**e**) and 150 K (**f**), which are marked by the color-coded arrows in (**a**). **g**, Large-scale STM topography at 9K. **h**, The corresponding FFT of (**g**). The green and red circles mark the Bravais vectors (a^* and b^*) of the pristine ab -plane layer, respectively. The orange circles mark the Bravais vectors ($q^* = a^*/3$) of the triple stripe charge order. **i**, High-resolution STM image for the 3×1 supercell of the triple-cube CDW. **j**, STS spectra of the uT, O and dT cube units, showing a charge order gap of ~ 0.17 eV. (g) scale bar, 5nm, $V_s = +1.2$ V; (h) scale bar, 2nm, $V_s = +1.2$ V.

A further zoomed-in image (Fig. 2i) depicts the additional order of sequentially-emerged electrical polarization along the b -axis (Supplementary Fig. S5). Particularly,

in each period of the stripe, three chains of ATS cubes show “up-triangular” (uT), “olive-shaped” (O) and “down-triangular” (dT) shapes in the occupied state, respectively. Figure 2j shows the chain-specific conductance (dI/dV) spectra obtained on the uT, O and dT chains, respectively. All of them show a quasi-gap of ~ 0.17 eV around the Fermi level (Supplementary Fig. S6) below 120 K, suggesting their CDW characteristics. We thus term it triple-cube CDW (tc-CDW) in the following discussion. The density of states (DOS) within the gap are not completely suppressed, suggesting the tc-CDW, most likely, occurs on the surface or even in a surface direction of the ATS crystal while the rest portion remains metallic. Such temperature dependent bandgap was verified in our low temperature ARPES measurements, as elucidated later.

Electronic structures of ATS and likely origin of tc-CDW

Two kinds of charge orders sequentially emerged around the transition temperature, namely the tc-CDW order along the a -axis and an electrical polarization along the b -axis (Supplementary Fig. S7). Figure 3a illustrates the surface 2D Brillouin zone (BZ) of a bulk ATS, imposed with its real-space lattice vectors and an atomic model. Figure 3b depicts its electronic band structures along high-symmetric directions. Bands 1-4 appear nearly flat along $\Gamma - X$, meanwhile they are highly dispersive and cross the Fermi level (E_F) along $\Gamma - Y$, explicitly showing the anisotropy of the inter-cube interactions. These four bands are the inter-cube bonding states along the b -axis and being hybridized between four pairs of Te atoms on the two facing planes of two adjacent cubes (Supplementary Fig. S8). Band 5 (orange) intersects band 3 (light green), opening a small gap of ~ 20 meV, at roughly $1/3 \Gamma - X$. Its band width along $\Gamma - X$ approaches 0.86 eV but is 0.36 eV in the $\Gamma - Y$ direction, indicating its stronger inter-cube interactions along $\Gamma - X$ (across chains). The anisotropy of inter-cube interactions of band 5 was confirmed by its wavefunction norm, depicting an inter-chain Te...Te bonding state and nearly isolated ATS cubes within the chain.

These five bands are thus categorized into two groups of highly anisotropic bands according to the plotted band structures and visualized wavefunction norms, which are illustrated in the plot of Fermi surface (FS) shown in Fig. 3c. As we elucidated later,

band 5 is occupied at the Y point in our experiments, which adjusts our E_F 61 meV higher than the DFT one. We thus plotted the FS at the adjusted E_F . Fermi surface sheets, comprised of bands 1-4, are parallel $\Gamma - X$ and intersect with a large vertically aligned ellipse originating from band 5, leading to several intersections. At those intersections, multiple “hot-spots” were formed showing bandgaps and embed a small closed ellipse comprised of bands 3 and 5. Those hot-spots are connected by vectors nearly parallel to the $\Gamma - X$ direction (red arrows) and their lengths are very close to $1/3 \Gamma - X$. We also calculated the electronic band structure and the FS of a monolayer model. It exhibits comparable electronic structures, i.e. highly anisotropic bands 1-5 showing intersecting Fermi surface sheets and ellipse, which indicates a weak interlayer electronic coupling in ATS crystals (Supplementary Fig. S9).

The tc-CDW may stem from electron-phonon coupling and/or electron correlation. Our DFT calculations do not find a significantly trimerized structure in either the bulk or the monolayer model and the Kohn anomaly⁴² was not clearly observed at a smearing energy less than $1 k_B T$. This implies that electron correlation, most likely, play a major role in forming the tc-CDW. Strong electron-electron interactions between band 5 and bands 1-4 and/or within band 5 were evidenced by the vectors connecting those pairs of hot-spots and the large joint density of states (JDOS) originated from the intersecting region. Most of the corresponding vectors are very close to $1/3 \Gamma - X$. Thus, the observed tc-CDW is, most likely, ascribed to strong inter-chain Coulomb interaction among ATS super-atoms through Te...Te quasi-bonding in the middle sub-layer and significant electron hopping along ATS chains through Te...Te non-covalent interactions in all sub-layers. In addition, those two categories of anisotropic bands, i.e. bands 1-4 versus band 5, also indicate superiorly stronger inter-cube interactions within the chains (along the b -axis). Therefore, each chain can be qualitatively regarded as one super-site in a 1D FS nesting model along the a -axis (Supplementary Fig. 10), and thus tending to form a quasi-1D CDW⁴³⁻⁴⁵ along that direction.

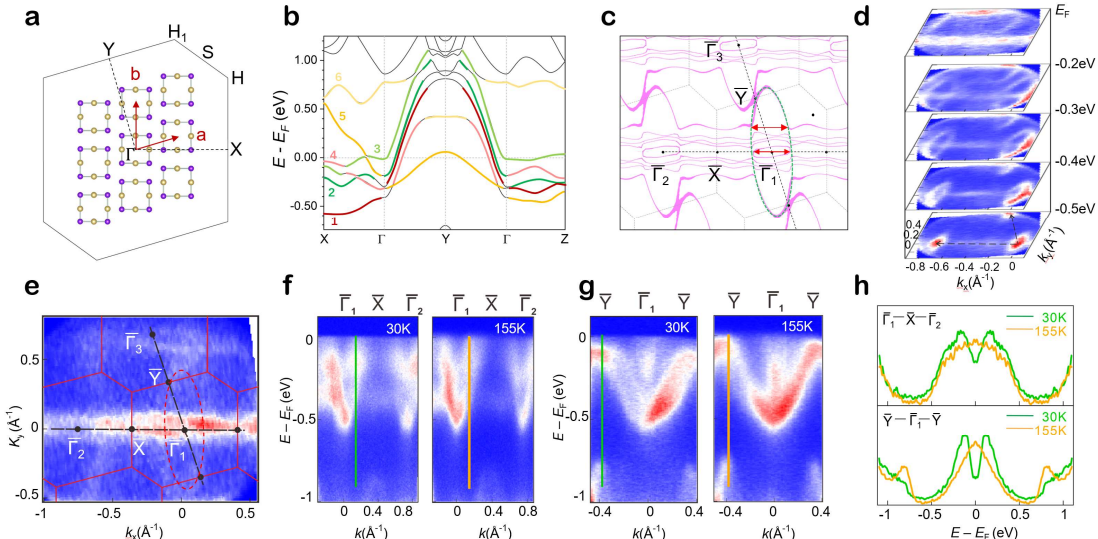


Figure 3. Electronic structure of the surface of ATS crystal. **a**, Two-dimensional Brillouin zone (BZ) of the surface (the *ab*-plane) of an ATS crystal and the corresponding structural model in real space. The *a* and *b* represent the lattice vectors. **b**, Theoretical band structure of bulk ATS along high-symmetric lines. Bands 1-6 were numbered according to their orders of eigen-energies at the *X* point and the color-code represent their wave-function components being categorized into three types, i.e., 1-4, 2-3 and 5-6 (Supplementary Fig. S8). **c**, Constant energy contours in the 2D Brillouin zone ($k_z = 0$) at the adjacent Fermi level with an energy broadening of ± 2 meV. The red arrows indicate two typical nesting vectors relevant with the tc-CDW. **d**, Constant-energy intensity plots with respect to the Fermi level obtained from ARPES measurements. Two high symmetry paths ($\Gamma - X - \Gamma$ and $\Gamma - Y - \Gamma$) are indicated using two black dashed lines at -0.5 eV plane. **e**, Integrated intensity plot with $E_F \pm 40$ meV. The large elliptical FS was marked using a red Dashed line. **f,g**, Two-dimensional intensity plots measured along $\Gamma_2 - \bar{X} - \Gamma_1$ (**f**) and $\bar{Y} - \Gamma_1 - \bar{Y}$ (**g**) at $T = 30$ K (left) and $T = 155$ K (right), respectively. **h**, The symmetrized energy distribution curves at 1/3 ($\Gamma - X$) and the *Y* point from (**f**) and (**g**), as measured at 30 K (green) and 155 K (orange), respectively.

While our DFT results indicate that both strong Coulomb interactions and significant electron hopping could be utilized through non-covalent interactions in the ATS layer, the predicted electronic structures were experimentally verified using ARPES measurements. Figure 3d shows constant-energy plots from E_F to 0.5 eV below E_F at $T=30$ K. It shows two converged points in the intensity map acquired at -0.5 eV, which are the Γ_1 and Γ_2 points of two adjacent BZs. Determination of the $\bar{\Gamma}$ point position further allows to derive the positions of high symmetry lines $\bar{\Gamma} - \bar{Y}$ and $\bar{\Gamma} - \bar{X}$ and the BZ boundary. Fig. 3e plots the intensity map at E_F where the 2D BZ boundary is highlighted using red solid lines. The large elliptical Fermi surface (indicated by the red dashed lines) and the relatively flat Fermi sheets along $\bar{\Gamma} - \bar{X}$ were clearly

resolved, highly consistent with the calculated FS shown in Fig. 3c.

Band dispersion measurements were performed at $T = 30$ and 155 K, respectively, to clarify the origin of the partial gap found in STS. Two cuts along high symmetry lines $\bar{\Gamma}_1 - \bar{X} - \bar{\Gamma}_2$ and $\bar{Y} - \bar{\Gamma}_1 - \bar{Y}$ are presented in Fig. 3f and 3g, respectively. Along $\bar{\Gamma}_1 - \bar{X} - \bar{\Gamma}_2$, a dispersive band (band 5) crosses the Fermi level near $1/3 \bar{\Gamma} - \bar{X}$ at 155 K, and is gapped out at 30 K. Along $\bar{Y} - \bar{\Gamma}_1 - \bar{Y}$, it reaches the Fermi level near the \bar{Y} point at 155 K, and is gapped out at 30 K as well. The gap openings along the two lines were more clearly illustrated using symmetrized energy distribution curve cuts, as shown in Fig. 3h. The determined gap size is ~ 135 meV (at 30 K), comparable with the STS result of ~ 0.17 eV (at 9 K).

Interweaving polar electronic states

Electrical polarization along the b -axis was clearly resolved in STM imaging, which is relevant with the breaking degeneracy of inter-cubic Te...Te interactions within ATS chains that reduces the joint-DOS near the Y point (Fig. 3b and 3c). Figure 4a and 4b show high-resolution STM images of the filled and empty states of the (uT-O-dT) tri-cube, respectively. It is remarkable that the directions of each triangular chain (uT & dT) are oppositely oriented to each other in the filled- and empty-states images, indicating the polarization along the b -axis is relevant with electronic hybridization, while no polarization occurs in the cubes of O chains. Figure 4c-4e provides a cartoon showing electronic dipoles formed, ascribed to charge polarization within the uT and dT cubes along the b -axis. The dipoles are parallel aligned within the uT and dT chains, but antiparallel oriented between uT and dT chains (Supplementary Fig. 11).

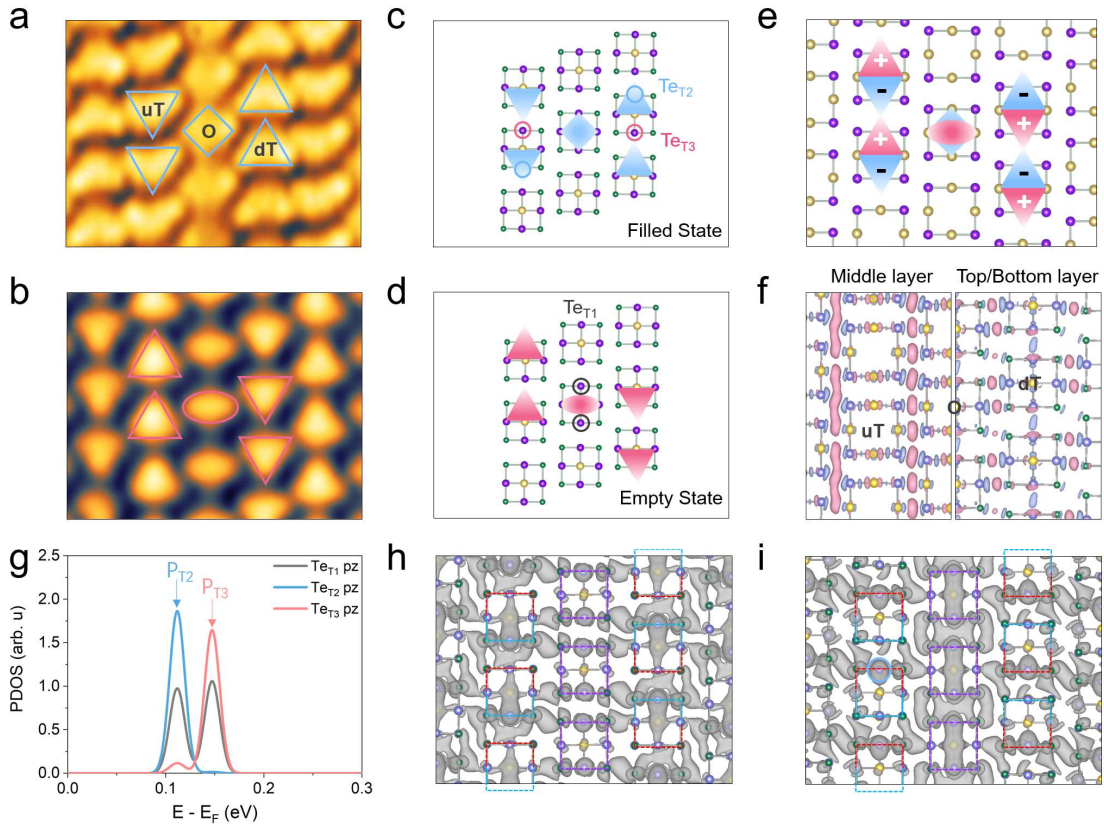


Figure 4. Antipolar electronic states of ATS cubes. **a,b**, STM topographic images of the ATS cubes at filled (**a**) and empty states (**b**), respectively. (**a**) scale bar 2nm, $V_s = +1.2V$; (**b**) scale bar 2nm, $V_s = -1.2V$. They show inter-chain bonding- (**c**) and antibonding-like (**d**) states among the (uT-O-dT) tri-cube. **e**, Illustration of polarized electronic states at filled and empty states. **f**, Inter-chain differential charge density (DCD) of an ATS monolayer where red and blue contours represent charge accumulation and depletion, respectively. Slabs of middle and top/bottom are shown in the left and right panels, respectively. The isosurface value is $0.0005 e/\text{Bohr}^3$. **g**, Projected density of states (PDOS) of p_z orbitals of three types of Te atoms, as denoted in (**c**) and (**d**), in the top sub-layer. **h,i**, Wavefunction norms of states P_{T2} (**h**) and P_{T3} (**i**), respectively, where the dashed boxes outline ATS cubes.

Appreciably accumulated (depleted) DOS was found at the uT-O and O-dT inter-chain regions in the filled-state (empty-state) image (Fig. 4a and 4b), indicating inter-chain electronic hybridization plays an essential role in resulting these polarized electronic states. Figure 4f depicts inter-chain differential charge density (DCD) in the middle (left) and top/bottom (right) sublayers of an ATS monolayer in the triple-cube stripe configuration. The middle sublayer appears the power house for inter-chain interactions where strong covalent-like Te...Te hybridizations, i.e. charge reduction (blue) near Te atoms and charge accumulation (red) in between them, were identified

at the inter-chain region. On the top sublayer, we observe promoted inter-chain Te...Se covalent-like characteristics and slightly weakened intra-chain Te...Te interactions, as reflected by charge accumulation at the inter-chain areas and charge reduction at the inter-cube region within chains, respectively.

Electronic interactions, primarily hybridization, are capable of introducing spatially polarized distribution of electronic states along the *b*-axis in the uT and dT chains, which are clearly evidenced by the projected DOS (PDOS) of Te atoms at the top-sublayer (Fig. 4g-4i and Supplementary Fig. 7). In comparison with atom Te_{T1} from the non-polarized O-chain, atoms Te_{T2} and Te_{T3} of the uT and dT chains display an apparent inversion-symmetry breaking. Representative peaks P_{T2} and P_{T3}, separated by 35 meV, both distribute on Te_{T1} and are preferably located on Te_{T2} and Te_{T3}, respectively, showing significant polarization in the uT and dT chains. Real-space wavefunction norms of these two peaks are visualized in Fig. 4h and 4i, which display strongly polarized states (inversion-symmetry breaking) along the *b*-axis in the uT and dT chains and inversion-symmetric states for the O-chain.

Discussion

The tc-CDW (along the *a*-axis) essentially enhances the uT-O and O-dT across-chain interactions that strengthen electronic hybridization in the across-chain direction, in which the inversion symmetry maintains for an O-chain cube. This reinforced hybridization tends to reduce the high DOS near the Y point and to lift the degeneracy of inter-cube electronic states within chains. As a consequence, polarized electronic states (along the *b*-axis) are thus correlatedly formed at low temperature. An anti-parallel polarized configuration is thus locked to ensure the inversion symmetry of the O cube being maintained. In other words, the specific anti-polarization configurations are selectively determined by the tc-CDW charge order; this is thus the reason why we term them interweaving polar charge orders.

Spatially polarized metallic states were originally proposed by P. W. Anderson and E. I. Blount in 1965⁴⁶. Until now, roughly 40 kinds of polar metallic materials have been theoretically predicted⁴⁷, while only very few of them have been discovered and

confirmed in experiments⁴⁸⁻⁵⁰. Nevertheless, an *anti*-polar metallic state was discovered in this work, primarily ascribed to strong electronic interactions rather than spatially displacements of atoms, which will, we believe, be promoting extensive theoretical and experimental studies in this field.

In short, we demonstrated that strong electron-electron interactions are at play in a non-covalently bonded 2D super-atomic layer. Such exceptionally strong interaction leads to the tc-CDW, the spatial polarization of electronic states and their interweaving anti-polar configuration of metallic states. These findings manifest that super-atomic layers, comprised with atomic clusters through non-covalent interactions, are capable for our novel playground of exploration, manipulation and utilization of exotic electronic properties which were usually investigated in covalently bonded solids. Given the high and precise turnability of super atoms, we would expect more super-atomic solids and layers were rationally designed by tailoring their super-atomic building blocks and inter-block interactions among them. It allows to explore those parameter regimes and thus observing emergent phenomena that were inaccessible in conventional quantum materials.

Methods

Sample preparation and STM measurements. Single crystals of $\text{Au}_6\text{Te}_{12}\text{Se}_8$ (ATS) were grown by the self-flux method. They are in shape of small platelets with shining mirror-like surfaces, typically $2 \times 4 \times 1 \text{ mm}^3$. The samples were cleaved in ultrahigh vacuum at room temperature, and subsequently cooled down for STM measurements. STM experiments were performed in a commercial variable-temperature STM (PanScan Freedom, RHK) operated in ultrahigh vacuum. Electrochemically etched polycrystalline tungsten calibrated on clean Au(111) surfaces were used for all our STM measurements tips. The STM topography was taken in the constant-current mode, and the dI/dV spectra were collected using a standard lock-in technique with a modulation frequency of 999.1 Hz. The STM measurements was performed mostly at 9 K for the high-resolution imaging, and at variable temperatures (from 9K to Room Temperature) for the phase transition characterization.

XRD, SEM and transport measurements: Powder X-ray diffraction (PXRD) patterns of polycrystalline ATS were measured using a panalytical X'pert diffractometer with the Cu-K α anode ($\lambda = 1.5408 \text{ \AA}$). Scanning electron microscopy (SEM) images of the ATS single crystal was acquired in a Hitachi S-4800 FE-SEM. Electrical resistivity (ρ) was measured using the standard four-wire method in a PPMS (Quantum Design).

Raman measurements: Raman spectroscopy measurements were performed using a home-built low-wavenumber and variable-temperature Raman system equipped with a semiconductor laser ($\lambda=532$ nm), a $50 \times$ objective (numerical aperture 0.8) and a 600 lines mm^{-1} grating. The sample was placed into a cryostat (attocube800 systems AG, Germany). To prevent potential CDW phase transitions driven by laser irradiation, the laser irradiance was kept below $100 \mu\text{W}/\mu\text{m}^2$. Low-wavenumber Raman filters (Ondax Inc., USA) were used to achieve a cut-off Raman shift down to $\sim 10 \text{ cm}^{-1}$. The step size of Raman mapping was $1 \mu\text{m}$. All the peaks were calibrated with the Si peak at 520.7 cm^{-1} .

ARPES measurements: ARPES measurements were performed at Renmin University of China equipped with a Scienta DA30 analyzer, with photon energy of 10.05 eV, and the BL13U beamline of National Synchrotron Radiation Laboratory (NSRL) equipped with a Scienta R4000 analyzer. The energy and angular resolution were set to 10 meV and 0.3° , respectively. Clean surfaces for ARPES measurements were obtained by *in situ* cleaving the samples. Photoemission spectra presented in this work were recorded at $T=30 \text{ K}$ and 155 K using the photo energy from 21 to 45 eV, in a working ultrahigh vacuum better than $6 \times 10^{-11} \text{ Torr}$.

Theoretical calculations. Density functional theory calculations were performed using the generalized gradient approximation for the exchange-correlation potential, the projector augmented wave method^{51,52}, and a plane-wave basis set as implemented in the Vienna *ab-initio* simulation package (VASP)⁵³. Dispersion corrections were made at the van der Waals density functional (vdW-DF) level^{54,55}, with the optB86b functional for the exchange potential (optB86b-vdW)^{56,57}. The kinetic energy cut-off for the plane-wave basis was set to 700 and 350 eV for all geometric property and electronic structure calculations, respectively. Two k -meshes of $7 \times 7 \times 5$ and $7 \times 7 \times 1$ were used to sample the first Brillouin zone in structure optimizations of the bulk and monolayer $\text{Au}_6\text{Te}_{12}\text{Se}_8$ (ATS) crystals, respectively. The k -meshes were increased to $15 \times 15 \times 15$ and $15 \times 15 \times 1$ in electronic structure calculations. An even denser k -mesh of $30 \times 30 \times 1$ was used to plot the 2D Fermi surface of the bulk ($k_z = 0$) and monolayer crystals. A 3×1 supercell was used to model the ATS monolayer in the tc-CDW state, the Brillouin zone of which was sampled using a $2 \times 7 \times 1$ k -mesh for both structural optimizations and electronic structure calculations. A vacuum layer of 17 \AA was used to eliminate image interactions among adjacent supercells. The shape and volume of the supercell and all atomic positions were fully relaxed until the residual force per atom was less than $0.01 \text{ eV}/\text{\AA}$. A Methfessel-Paxton smearing of 0.05 eV and the Bloch corrected tetrahedron method were used for Brillouin zone integral in calculations of geometric and electronic structures, respectively. A Gaussian smearing of 0.01 eV was used to plot projected density of states for the 3×1 supercell. We calculated charge densities of three single ATS chains (i.e. ρ_{uT} , ρ_O and ρ_{dT}) using the same geometry and precision as those in the 3×1 supercell and subtracted them from total charge density of the supercell (ρ_{total}) to get the inter-chain differential charge density (ρ_{DCD}), *i.e.*, $\rho_{DCD} = \rho_{total} - \rho_{uT} - \rho_O - \rho_{dT}$.

Reference:

1. Kamihara, Y., Watanabe, T., Hirano, M. & Hosono, H. Iron-based layered superconductor $\text{La}[\text{O}_{1-x}\text{F}_x]\text{FeAs}$ ($x = 0.05\text{-}0.12$) with $T_c=26$ K. *J. Am. Chem. Soc.* **130**, 3296-3297, (2008).
2. Liu, Y. *et al.* Correlating crystallographic orientation and ferroic properties of twin domains in metal halide perovskites. *Acs Nano.* **15**, 7139-7148 (2021).
3. Etgar, L. *et al.* Mesoscopic $\text{CH}_3\text{NH}_3\text{PbI}_3/\text{TiO}_2$ heterojunction solar cells. *J. Am. Chem. Soc.* **134**, 17396-17399 (2012).
4. Huang, H. *et al.* Growth mechanism of strongly emitting $\text{CH}_3\text{NH}_3\text{PbBr}_3$ perovskite nanocrystals with a tunable bandgap. *Nat. Commun.* **8**, 996 (2017).
5. Handy, L. L. & Gregory, N. W. A study of the chromous-chromic iodide equilibrium. *J. Am. Chem. Soc.* **72**, 5049-5051 (1950).
6. Huang, B. *et al.* Layer-dependent ferromagnetism in a van der Waals crystal down to the monolayer limit. *Nature* **546**, 270-273 (2017).
7. Li, P. *et al.* Single-layer CrI_3 grown by molecular beam epitaxy. *Sci. Bull.* **65**, 1064-1071 (2020).
8. Gu, Q. *et al.* Single particle tunneling spectrum of superconducting $\text{Nd}_{1-x}\text{Sr}_x\text{NiO}_2$ thin films. *Nat. Commun.* **11**, 6027 (2020).
9. Jia, S. *et al.* Ferromagnetic quantum critical point induced by dimer-breaking in $\text{SrCo}_2(\text{Ge}_{1-x}\text{P}_x)_2$. *Nat. Phys.* **7** 207-210 (2011).
10. Hirai, D., von Rohr, F. & Cava, R. J. Emergence of superconductivity in $\text{BaNi}_2(\text{Ge}_{1-x}\text{P}_x)_2$ at a structural instability. *Phys. Rev. B* **86**, 100505(R) (2012).
11. Reifsnider, K. L., Raihan, R. & Q. Liu. Rational durability design of heterogeneous functional materials: some first principles. **49** 31-54 (2012).
12. Doud, E. A. *et al.* Superatoms in materials science. *Nat. Rev. Mater.* **5**, 371-387 (2020).
13. Zhao, Y. *et al.* Extraordinarily strong interlayer interaction in 2D layered PtS_2 . *Adv. Mater.* **28**, 2399-2407 (2016).
14. Qiao, J. *et al.* Few-layer tellurium: one-dimensional-like layered elementary semiconductor with striking physical properties. *Sci. Bull.* **63**, 159-168 (2018).
15. Zhao, Y. *et al.* High-electron-mobility and air-stable 2D layered PtSe_2 FETs. *Adv. Mater.* **29**, 1604230 (2017).
16. Qiao, J., Kong, X., Hu, Z.-X., Yang, F. & Ji, W. High-mobility transport anisotropy and linear dichroism in few-layer black phosphorus. *Nat. Commun.* **5**, 4475 (2014).
17. Guo, P. J., Lu, X. Q., Ji, W., Liu, K. & Lu, Z. Y. Quantum spin Hall effect in monolayer and bilayer TaIrTe_4 . *Phys. Rev. B* **102**, 041109 (2020).
18. Jiang, P. *et al.* Stacking tunable interlayer magnetism in bilayer CrI_3 . *Phys. Rev. B* **99**, 144401 (2019).
19. Sivadas, N., Okamoto, S., Xu, X., Fennie, C. J. & Xiao, D. Stacking-dependent magnetism in bilayer CrI_3 . *Nano. Lett.* **18**, 7658-7664 (2018).
20. Gao, Y., Wu, M. & Jena, P. A family of ionic supersalts with covalent-like directionality and unconventional multiferroicity. *Nat. Commun.* **12**, 1331 (2021).
21. Guo, J., Qi, Y., Matsuishi, S. & Hosono, H. T_c maximum in solid solution of pyrite $\text{IrSe}_2\text{-RhSe}_2$ induced by destabilization of anion dimers. *J. Am. Chem. Soc.* **134**, 20001-20004 (2012).
22. Geim, A. K. & Grigorieva, I. V. Van der Waals heterostructures. *Nature* **499**, 419-425 (2013).
23. Cheng, Y., Huang, C., Hong, H., Zhao, Z. & Liu, K. Emerging properties of two-dimensional twisted bilayer materials. *Chin. Phys. B* **28**, 1674-1056 (2019).

24. Gonzalez, R. I. *et al.* Bending energy of 2D materials: graphene, MoS₂ and imogolite. *Rsc Adv.* **8**, 4577-4583 (2018).

25. Kusmartseva, A. F., Sipos, B., Berger, H., Forro, L. & Tutis, E. Pressure induced superconductivity in pristine 1T-TiSe₂. *Phys. Rev. Lett.* **103**, 236401 (2009).

26. Han, W. *et al.* Two-dimensional inorganic molecular crystals. *Nat. Commun.* **10**, 4728, (2019).

27. Voevodin, A., Campos, L. M. & Roy, X. Multifunctional vesicles from a self-assembled cluster-containing diblock copolymer. *J. Am. Chem. Soc.* **140**, 5607-5611 (2018).

28. Castleman Jr., A. W. & Puru J. Clusters: a bridge across the disciplines of environment, materials science, and biology. *PNAS* **103**, 10560–10569 (2006).

29. Puru J. & Qiang S. Super atomic clusters: design rules and potential for building blocks of materials. *Chem. Rev.* **118**, 5755-5870 (2018).

30. Puru J. & Qiang S. Theory-guided discovery of novel materials. *J. Phys. Chem. Lett.* **12**, 6499–6513 (2021).

31. Maliakal, A., Raghavachari, K., Katz, H., Chandross, E. & Siegrist, T. Photochemical stability of pentacene and a substituted pentacene in solution and in thin films. *Chem. Mater.* **16**, 4980-4986 (2004).

32. Cui, X. *et al.* Realizing nearly-free-electron like conduction band in a molecular film through mediating intermolecular van der Waals interactions. *Nat. Commun.* **10**, 3374, (2019).

33. Li, G. *et al.* Self-assembly of C₆₀ monolayer on epitaxially grown, nanostructured graphene on Ru(0001) surface. *Appl. Phys. Lett.* **100**, 013304 (2012).

34. Anderson, P. W. The resonating valence bond state in La₂CuO₄ and superconductivity. *Science* **235**, 1196-1198 (1987).

35. Guo, J. *et al.* Superconductivity in the iron selenide K_xFe₂Se₂ (0 <= x <= 1.0). *Phys. Rev. B* **82**, 180520 (2010).

36. Ang, R. *et al.* Real-space coexistence of the melted mott state and superconductivity in Fe-substituted 1T-TaS₂. *Phys. Rev. Lett.* **109**, 176403, (2012).

37. Guo, J. G. *et al.* Quasi-two-dimensional superconductivity from dimerization of atomically ordered AuTe₂Se_{4/3} cubes. *Nat. Comm.* **8**, 871, (2017).

38. Jia, X. Y. *et al.* Nodeless superconductivity in a quasi-two-dimensional superconductor AuTe₂Se_{4/3}. *Chin. Phys. B* **27**, 067401, (2018).

39. Fang, A., Ru, N., Fisher, I. R. & Kapitulnik, A. STM studies of TbTe₃: Evidence for a fully incommensurate charge density wave. *Phys. Rev. Lett.* **99**, 046401, (2007).

40. Malliakas, C., Billinge, S. J. L., Kim, H. J. & Kanatzidis, M. G. Square nets of tellurium: Rare-earth dependent variation in the charge-density wave of RETe₃ (RE = rare-earth element). *J. Am. Chem. Soc.* **127**, 6510-6511, (2005).

41. Denholme, S. J. *et al.* Coexistence of superconductivity and charge-density wave in the quasi-one-dimensional material HfTe₃. *Sci. Rep.* **7**, 45217, (2017).

42. Kohn, W. Image of the fermi surface in the vibration spectrum of a metal. *Phys. Rev. Lett.* **2**, 393-394 (1959).

43. Zhu, X., Guo, J., Zhang, J. & Plummer, E. W. Misconceptions associated with the origin of charge density waves. *Adv Phys.* **2**, 622–640, (2017)

44. Gruner, G. in *Density waves in solids*, vol. **89**, (Addison-Wesley Publishing Company, Massachusetts, 1994).

45. Peierls, R. E. Quantum theory of solids. (1955).
46. Anderson, P. W. B., E. I. Symmetry considerations on martensiti“ transformati”ns: "ferroelectric" metals? *Phys. Rev. Lett.* **14**, 532 (1965).
47. Zhou, W. X. & Ariando, A. Review on ferroelectric/polar metals. *Jpn. J. Appl. Phys.* **59**, SI0802 (2020).
48. Fei, Z. *et al.* Ferroelectric switching of a two-dimensional metal. *Nature* **560**, 336-339 (2018).
49. Sharma, P. *et al.* A room-temperature ferroelectric semimetal. *Sci. Adv.* **5**, eaax5080 (2019).
50. Kim, T. H. *et al.* Polar metals by geometric design. *Nature* **533**, 68-71 (2016)
51. Blochl, P. E. Projector augmented-wave method. *Phys. Rev. B* **50**, 17953-17979 (1994).
52. Kresse, G. & Joubert, D. From ultrasoft pseudopotentials to the projector augmented-wave method. *Phys. Rev. B* **59**, 1758-1775 (1999).
53. Kresse, G. & Furthmuller, J. Efficient iterative schemes for ab initio total-energy calculations using a plane-wave basis set. *Phys. Rev. B* **54**, 11169-11186 (1996).
54. Lee, K., Murray, E. D., Kong, L., Lundqvist, B. I. & Langreth, D. C. Higher-accuracy van der Waals density functional. *Phys. Rev. B* **82**, 081101 (2010).
55. Dion, M., Rydberg, H., Schroder, E., Langreth, D. C. & Lundqvist, B. I. Van der Waals density functional for general geometries. *Phys. Rev. Lett.* **92**, 246401 (2004).
56. Klimes, J., Bowler, D. R. & Michaelides, A. Van der Waals density functionals applied to solids. *Phys. Rev. B* **83**, 195131 (2011).
57. Klimes, J., Bowler, D. R. & Michaelides, A. Chemical accuracy for the van der Waals density functional. *J. Phys. Condens. Matter* **22**, 022201 (2010).

Acknowledgments

This project is supported by the National Natural Science Foundation of China (NSFC) (No. 61674045, 11604063, 61911540074, 51922105, 11774421, 61761166009, 11974422), the Ministry of Science and Technology (MOST) of China (No. 2016YFA0200700, 2018YFE0202700), the Strategic Priority Research Program (Chinese Academy of Sciences, CAS) (No. XDB30000000). Z.H. Cheng was supported by the Fundamental Research Funds for the Central Universities and the Research Funds of Renmin University of China (No. 21XNLG27). Calculations were performed at the Physics Lab of High-Performance Computing of Renmin University of China, Shanghai Supercomputer Center.

Author contributions

Z.C., S.W., J.G. and W.J. conceived the research project. S.X. L.L., Q.Z., X.L., L.H., H.J.G. and Z.C. performed the STM experiments and analysis of STM data. Z.W. and S.W. performed the ARPES experiments and analysis of ARPES data. X.C., J.G. and X.C. grew the single crystals and performed transport, SEM and XRD measurements. H.L., S.H., S.C. and L.X. performed Raman measurements. L.W., L. Z. and W.J. performed the DFT calculations. S.X., L.W., Z.W., Z.C. S.W. and W.J. wrote the manuscript with inputs from all authors.

Supporting Materials

Interweaving polar charge orders in a layered metallic super-atomic crystal

Shuya Xing^{1,†}, Linlu Wu^{1,†}, Zilu Wang^{1,†}, Xu Chen^{2,†}, Haining Liu^{3,4}, Shuo Han¹, Le Lei¹, Linwei Zhou¹, Qi Zheng^{2,4}, Li Huang^{2,4}, Xiao Lin⁴, Shanshan Chen¹, Liming Xie^{3,4}, Xiaolong Chen^{2,4,5} Hong-Jun Gao^{2,4}, Zhihai Cheng^{1,*}, Jiangang Guo^{2,5,*}, Shancai Wang^{1,*}, and Wei Ji^{1,*}

¹*Beijing Key Laboratory of Optoelectronic Functional Materials & Micro-nano Devices,*

Department of Physics, Renmin University of China, Beijing 100872, China

²*Beijing National Laboratory for Condensed Matter Physics, Institute of Physics, Chinese*

Academy of Sciences, P.O. Box 603, Beijing 100190, China.

³*CAS Key Laboratory of Standardization and Measurement for Nanotechnology, CAS*

Centre for Excellence in Nanoscience, National Centre for Nanoscience and Technology,

Beijing 100190, China

⁴*University of Chinese Academy of Sciences, Beijing 100039, China*

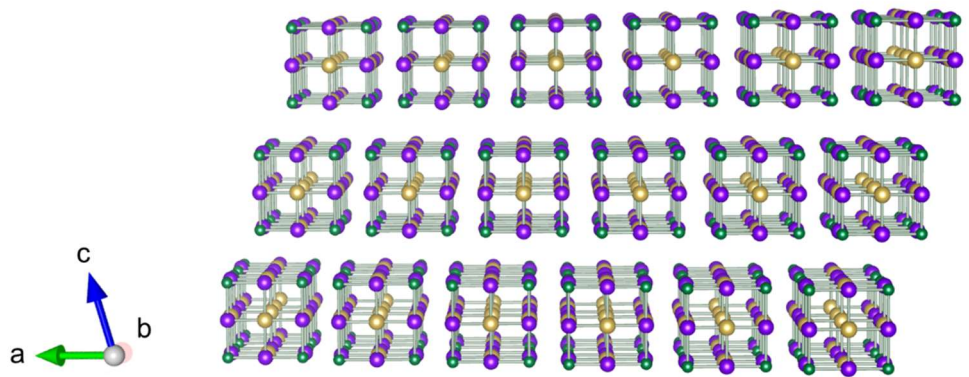
⁵*Songshan Lake Materials Laboratory, Dongguan, Guangdong 523808, China*

[†] These authors contributed equally: Shuya Xing, Linlu Wu, Zilu Wang, Xu Chen.

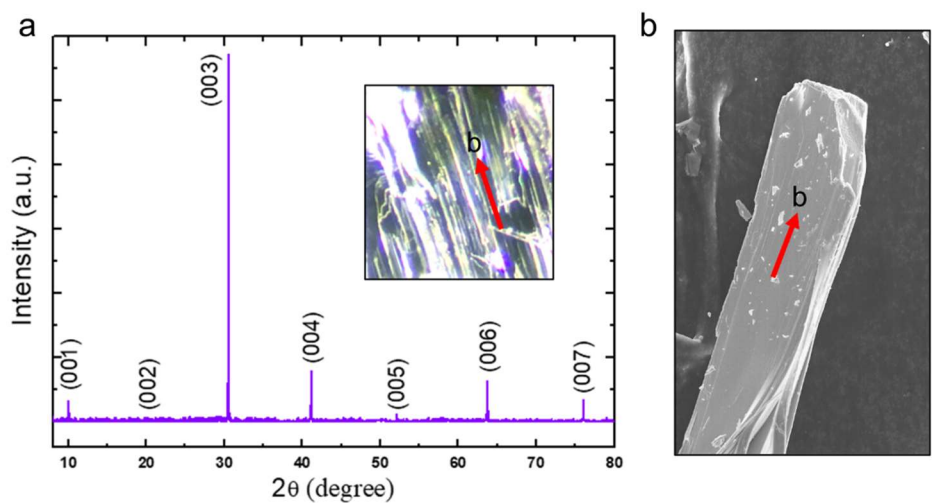
* Email: zhihaicheng@ruc.edu.cn jgguo@iphy.ac.cn scw@ruc.edu.cn wji@ruc.edu.cn

Table of Contents

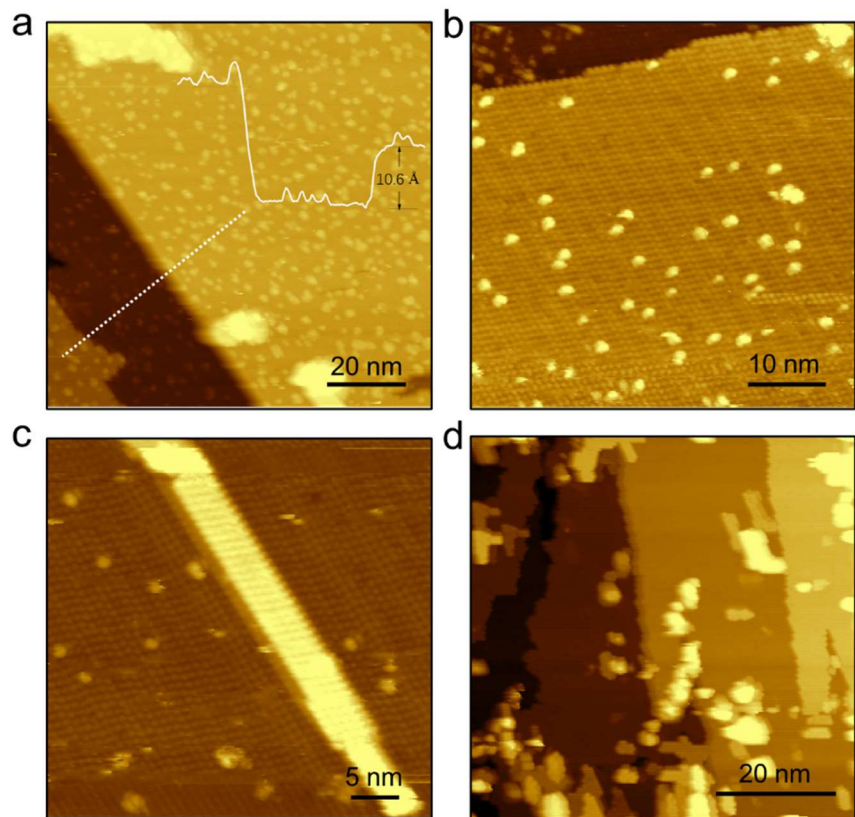
- **Supplementary Figure 1.** Three-dimensional stacking structure of the layered super-atomic crystal of $\text{AuTe}_2\text{Se}_{4/3}$ (ATS).
- **Supplementary Figure 2.** Structure and morphology characterization of ATS crystal.
- **Supplementary Figure 3.** STM topography of the cleaved ATS surface.
- **Supplementary Figure 4.** Temperature-dependent transport measurements of charge order transition in ATS.
- **Supplementary Figure 5.** Bias polarity-specific STM images.
- **Supplementary Figure 6.** STS spectra of ATS at ~ 150 K (above the charge order transition temperature).
- **Supplementary Figure 7.** STM topography and atomic resolution images of ATS at the triple-cube CDW.
- **Supplementary Figure 8.** Projected band dispersion and visualized wave function norms of bulk ATS.
- **Supplementary Figure 9.** Fermi surface and projected band dispersion of pristine monolayer ATS.
- **Supplementary Figure 10.** Schematic mechanism of 1D charge density wave (CDW) in reciprocal space
- **Supplementary Figure 11.** Schematic mechanism of dipole formation and polar states.
- **Supplementary Figure 12.** Schematic symmetry-reducing process in the geometry and electronic structure of the layered $\text{AuTe}_2\text{Se}_{4/3}$ super-atomic crystal.



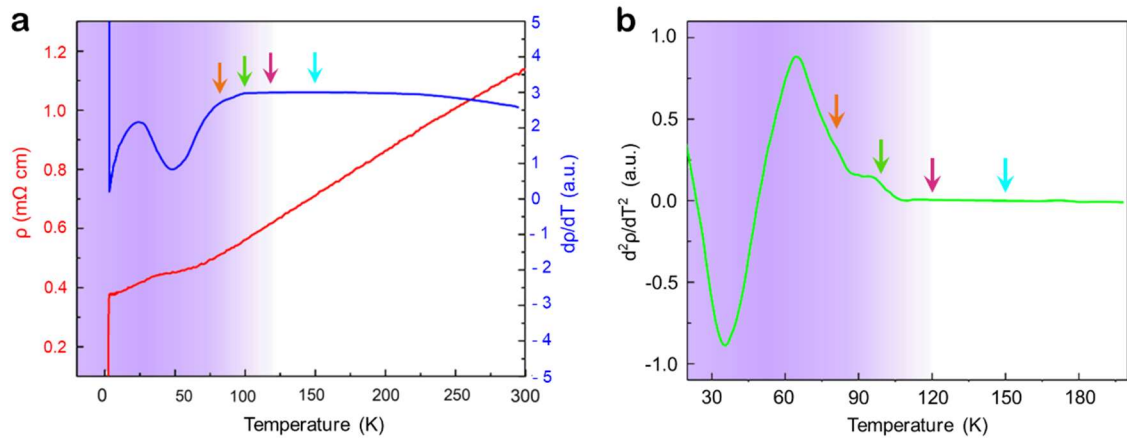
Supplementary Figure 1. Three-dimensional stacking structure of the layered super-atomic crystal of $\text{AuTe}_2\text{Se}_{4/3}$ (ATS) crystal. The 2D layers in the ab -plane are stacked along the c -axis with the relative weak Van der Waals interactions.



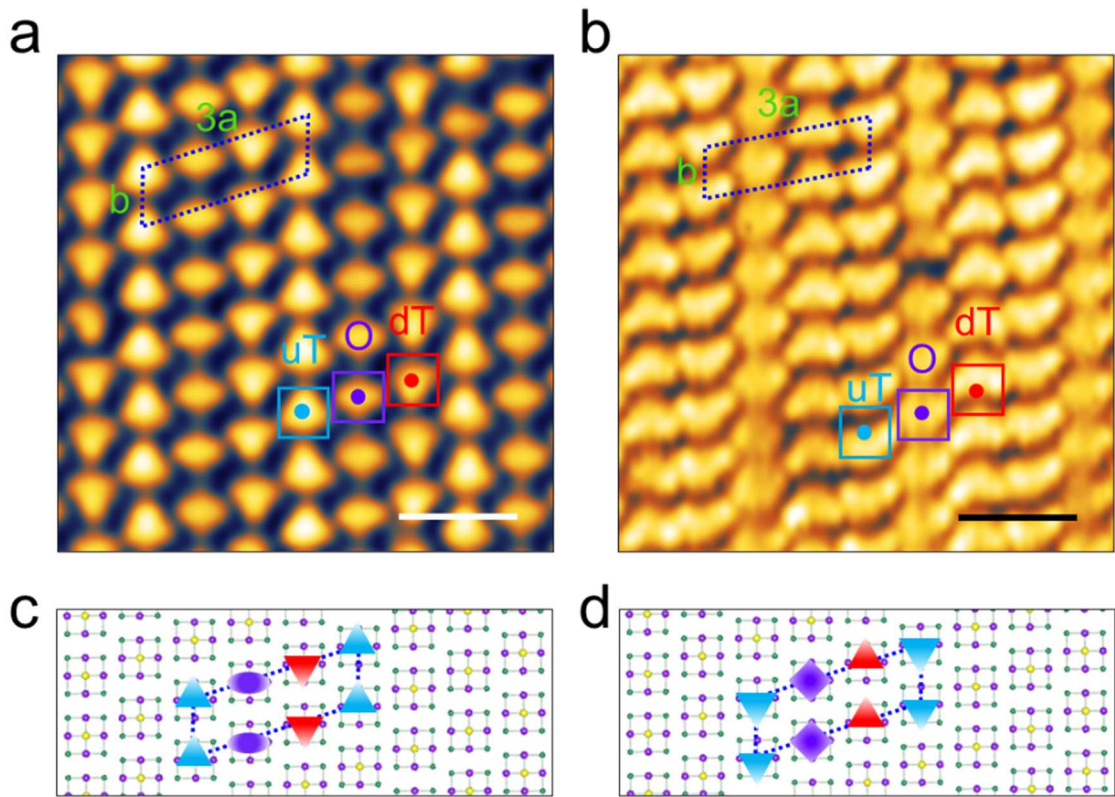
Supplementary Figure 2. Structure and morphology characterization of $\text{AuTe}_2\text{Se}_{4/3}$ (ATS) crystal. **a**, The X-ray diffraction (XRD) pattern of ATS single crystal only shows [001] Bragg peaks, indicating that the *ab*-plane is the cleaving plane of ATS crystal. The inset is the optical image of the cleaved ATS single crystal. The major step direction of the cleaved plane is along the *b*-axis, reflecting the in-plane anisotropy of the *ab*-plane. **b**, SEM image of a strip of ATS single crystal. The *b*-axis of the crystal is marked in both optical and SEM images.



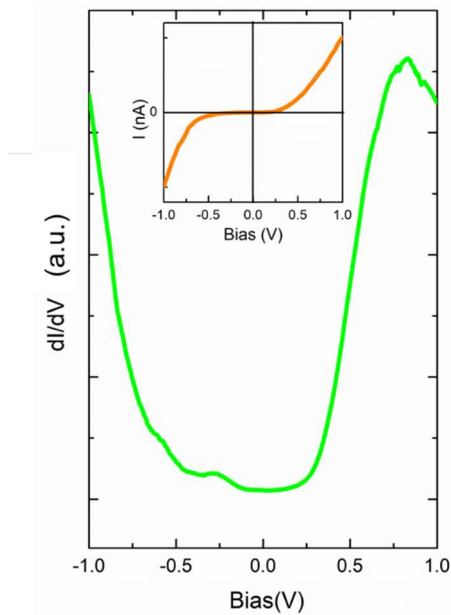
Supplementary Figure 3. STM topography of the cleaved ATS surface. **a**, Large-scale STM image of terraces with step edges and small patches on the terraces. The line-scan profile taken along the white dotted line indicate the single-layer and double-layer step heights. **b**, High-resolution STM image of a terrace covered by the randomly distributed zero-dimensional ATS cubes (0D). **c**, High-resolution STM image of a terrace covered with a one-dimensional ATS nanoribbon (1D). **d**, The typical STM image of the cleaved surface, indicating the experimental difficulty due to the weak inter-cube interactions. Scanning parameters are **(a)** $V_s = 2.4$ V, **(b)** $V_s = 2.0$ V, **(c)** $V_s = 1.6$ V, **(d)** $V_s = 3.1$ V. The specific 0D-1D-2D structural nature of the ATS crystal can be readily confirmed through the above STM results. Based on the experimental experience, there is more chance to get the clean surface by mechanical cleaving along the direction vertical to the *b*-axis.



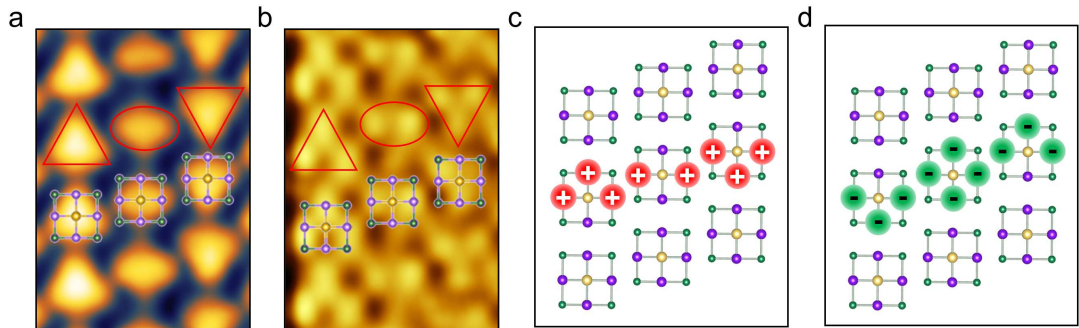
Supplementary Figure 4. Temperature-dependent transport measurements of the charge order transition in ATS. **a**, Temperature-dependent resistivity (red) and its temperature derivative (blue) curves of ATS. The hump-like feature at the temperatures below 120K indicates the sequential formation of the triple-cube CDW and the charge polarization. **b**, Second order derivative of temperature-dependent resistivity (green) curves. The kink-like feature at below 80K indicating the formation of the charge polarization.



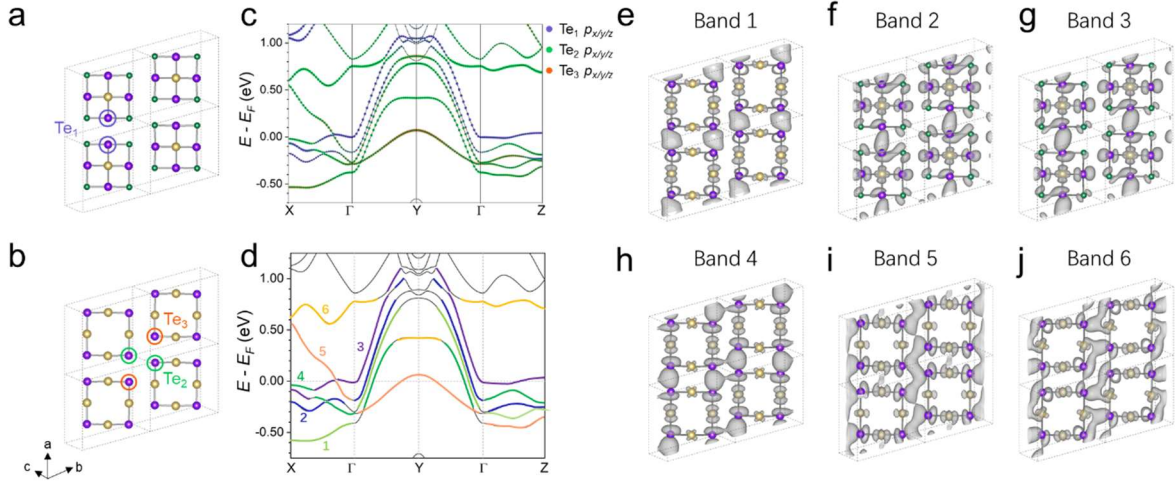
Supplementary Figure 5. Bias polarity-specific STM images. **a,b**, Bias-dependent STM images of empty **(a)** and unoccupied **(b)** states for the 1×3 supercell of triple-cube CDW. The supercell of the triple-cube CDW consists of a chain of ‘olive-shaped’ (O), ‘down-triangular’ (dT) and ‘up-triangular’ (uT) in **(a)**. **(c)** and **(d)** are the schematic models of **(a)** and **(b)**, respectively. **(a)** scale bar, 2nm, $V_s = 1.2$ V, **(b)** scale bar, 2nm, $V_s = -1.2$ V.



Supplementary Figure 6. STS spectra of ATS at ~ 150 K (above the charge order transition temperature). No density of states gap was observed in the STS spectra, which is clearly different from the corresponding STS spectra obtained at 9K.

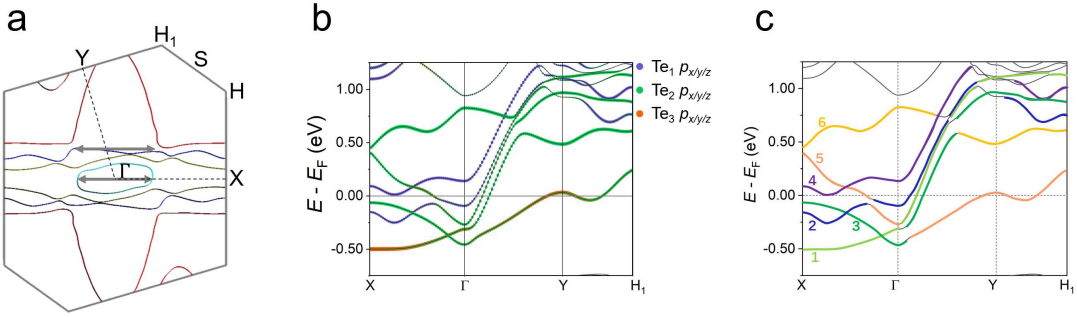


Supplementary Figure 7. STM topography and atomic resolution images of ATS at the triple-cube CDW. **a**, The regular STM topography image of the triple-cube CDW. The (uT-O-dT) cubes show the specific ‘up-triangular’(uT), ‘olive-shaped’ (O) and ‘down-triangular’ (dT) shapes, respectively. **b**, The atomic resolution image of the triple-cube CDW. Atomic structure of the cubes (top layer) was overlaid on the (uT-O-dT) cubes in **(a)** and **(b)**. **c,d**, The schematic structural models of the (uT-O-dT) cubes (top layer) for the triple charge order states obtained at positive **(a)** and negative bias **(b)**. **(a)** 2.5×3.5 nm, $V_s = +1.4$ V, **(b)** 2.5×3.5 nm, $V_s = +2.3$ V. The atomic-resolution images of ATS show that the difference of Te atoms along the *b*-axis of top layer is the reason for the symmetry-broken electronic states, as shown in **(a)** and **(b)**. At the positive bias, the ‘up-triangular’ (uT), ‘olive-shaped’ (O) and ‘down-triangular’ (dT) shapes are mainly contributed by the ‘up-three’ (uT), ‘middle-two’ (O) and ‘down-three’ (dT) Te atoms of top layer **(c)**. At the negative bias, the ‘down-triangular’ (uT), ‘rhombus-shaped’ (O) and ‘up-triangular’ (dT) shapes are mainly contributed by the ‘down-three’ (uT), ‘all-four’ (O) and ‘up-three’ (dT) Te atoms of top layer **(d)**.

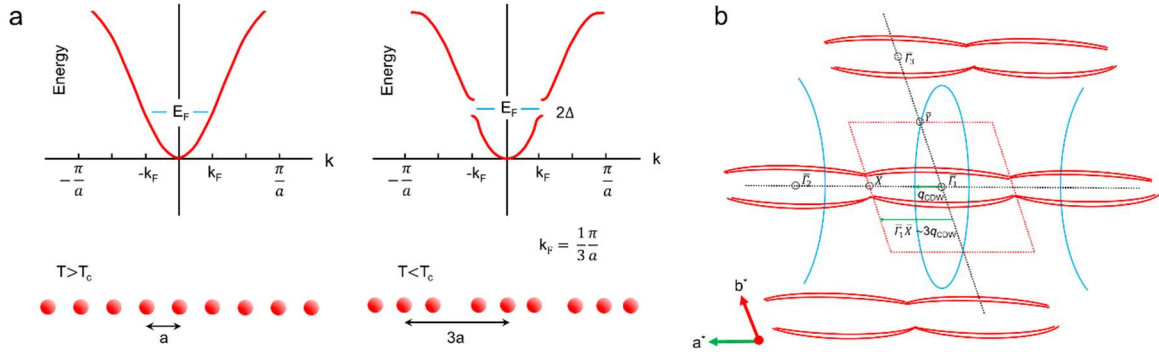


Supplementary Figure 8. Projected band dispersion and visualized wave-function norms of bulk ATS.

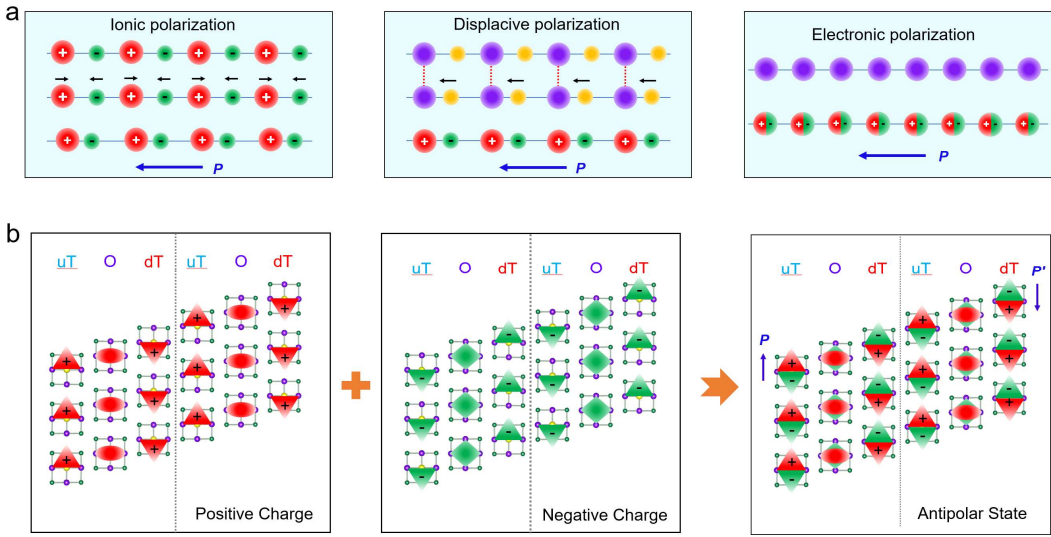
a, b, The top/bottom and middle sublayers of bulk ATS. Three kinds of Te atoms involved in inter-cube Te...Te interactions are labeled by purple, green and orange circles, respectively. Unit cell of lattice is labeled by black dash line. **c, d,** Electronic band structures of bulk ATS. The p orbitals of Te atoms in **(c)** are mapped with different colors: $\text{Te}_1-p_{x/y/z}$, purple; $\text{Te}_2-p_{x/y/z}$, green; $\text{Te}_3-p_{x/y/z}$, orange. Bands 1-6 in **(d)** were numbered according to their orders of eigen-energies at the X point and color-coded by their wave-function components, as shown in **(e)-(j)**. **(e)-(j)** Visualized wave-function norms of bands 1-6 at the Γ point. The wave-function components are categorized into three types, i.e., 1-4 (inter-cube Te_2 - Te_3 bonding states along the chain), 2-3 (inter-cube Te_1 - Te_1 bonding states along the chain) and 5-6 (inter-cube Te_2 - Te_3 bonding states across the chain). The isosurface value is 0.001 e/Bohr³.



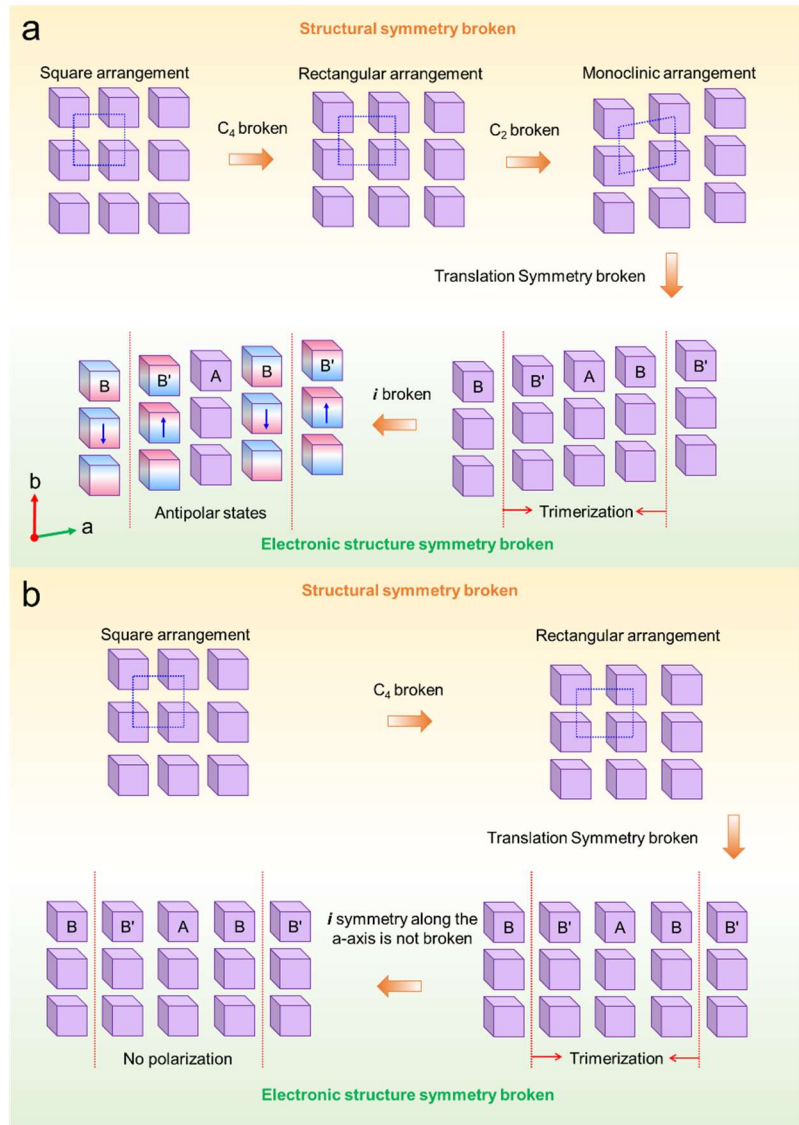
Supplementary Figure 9. Fermi surface and projected band dispersion of pristine monolayer ATS. **a**, Calculated Fermi surface of monolayer ATS with the four color-coded Fermi sheets. The possible nesting vectors of the triple-cube CDW are marked by the grey arrows. **b, c**, Electronic band structures of monolayer ATS. The p orbitals of Te atoms in **(b)** are mapped with different colors: $\text{Te}_1-p_{x/y/z}$, purple; $\text{Te}_2-p_{x/y/z}$, green; $\text{Te}_3-p_{x/y/z}$, orange. The definition of Te_{1-3} in monolayer is as same as that in bulk, as shown in Fig. S8 (a)-(b). Bands 1-6 in **(c)** were numbered according to their orders of eigen-energies at the X point and color-coded by their wave-function components.



Supplementary Figure 10. Schematic mechanism of 1D charge density wave (CDW) in reciprocal space. **a**, The schematic mechanism of a triple-cube CDW transition for 1D metal CDW with $k_F = 1/3 (\pi/a)$. **b**, the rough sketch of Fermi surface (according to the ARPES results in Fig. 3e) and formation mechanism of the triple-cube CDW in ATS. The red parallelogram represents the reciprocal lattice of the ab -plane. The Fermi surface consists of two parts: a pair of flat sheets (red) parallel to $\bar{F}_2 - \bar{X} - \bar{F}_1$ direction and an ellipse (blue) perpendicular to $\bar{F}_2 - \bar{X} - \bar{F}_1$. The half axis of the ellipse (along the a^* axis) is identified as q_{CDW} (the short green arrow), which is about 1/3 of $\bar{F}_1\bar{X}$ (the long green arrow). The q_{CDW} is considered as the nesting vector for the formation of the triple-cube CDW in ATS.



Supplementary Figure 11. Schematic mechanism of dipole formation and polar states. a, Ionic polarization: the relative displacements of the positively charged and negatively charged ions. Displacive polarization: the previous neutral atoms undergo a neutral-ionic transition due to their relative displacements. Electronic polarization: the polarization (charge separation) is due to the ordering of electrons. **b,** Schematic mechanism of electronic states in ATS due to the electronic polarization of super-atoms (cubes) along the *b*-axis and tripe CDW state along the *a*-axis in the low-symmetric *P1* lattice.



Supplementary Figure 12. Schematic symmetry-reducing process in the geometry and electronic structure of the layered ATS super-atomic crystal. a, the building block is the high-symmetric cube of ATS, which could form a layered geometric structure in a square arrangement. The square arrangement of cubes is reduced to rectangular arrangement and then monoclinic arrangement (*P1* symmetry) by the sequential breaking of *C*₄ and *C*₂ symmetry to minimize the directive inter-cube bonding/interaction energy. The translation symmetry of monoclinic arrangement (*P1* symmetry) is further broken to minimize the electronic energy via the formation of triple-cube CDW (along the *a*-axis). The inversion symmetry of B (and B') cubes is broken due to the trimerization of cube along the *b*-axis, then the electronic energy is further decreased via the polarization of B (and B') cubes and the formation of polarization states in the low-symmetric geometric structure. **b**, However, the inversion symmetry of B (and B') cubes along the *b*-axis is preserved for the rectangular arrangement (*C*₂ symmetry), which indicating that the low-symmetric geometry structure (monoclinic arrangement) is necessary to form the polarization states in ATS.